

Induction Motor Eccentricity Fault Analysis and Quantification with Modified Winding Function based Model

Wang, Bingnan; Albader, Mesaad; Inoue, Hiroshi; Kanemaru, Makoto

TR2022-153 December 03, 2022

Abstract

In this paper, we build a fast simulation model for the analysis of eccentric induction motor. The self and mutual inductances of the motor windings are calculated with modified winding function method, with slotting effect and core saturation considered for improved accuracy. The calculated inductances are then fed into a coupled circuit model to simulate the dynamics of an eccentric induction motor. Compared with time-stepping finite-element method, the model is much faster for machines under eccentric faulty conditions. The accuracy of the model is validated with experiment measurements, with good match for fault component amplitudes.

International Conference on Electrical Machines and Systems (ICEMS) 2022

Induction Motor Eccentricity Fault Analysis and Quantification with Modified Winding Function based Model

Bingnan Wang¹, Mesaad W. Albader^{1,2}, Hiroshi Inoue³, and Makoto Kanemaru³

¹*Mitsubishi Electric Research Laboratories, 201 Broadway, Cambridge, MA 02139, USA*

²*Dept. of Electrical & Computer Engineering, Texas A&M University, College Station, TX 77843, USA*

³*Advanced Technology R&D Center, Mitsubishi Electric Corporation, Amagasaki, Hyogo, 661-8661, Japan*

Abstract—In this paper, we build a fast simulation model for the analysis of eccentric induction motor. The self and mutual inductances of the motor windings are calculated with modified winding function method, with slotting effect and core saturation considered for improved accuracy. The calculated inductances are then fed into a coupled circuit model to simulate the dynamics of an eccentric induction motor. Compared with time-stepping finite-element method, the model is much faster for machines under eccentric faulty conditions. The accuracy of the model is validated with experiment measurements, with good match for fault component amplitudes.

I. INTRODUCTION

Among many different faults that can happen in a motor, eccentricity is one common fault that occurs when air gap between stator bore and the rotor is not uniform [1], [2], [3]. Eccentricity faults can be categorized into three types: static eccentricity, dynamic eccentricity, and mixed eccentricity. Static eccentricity occurs when the center of the rotor is displaced from the stator bore central axis, while the rotor rotation center is still aligned with the center of the rotor. Dynamic eccentricity occurs when the rotation center and the stator bore central axis still aligns, but the rotor center is displaced. Mixed eccentricity is a combination of both static eccentricity and dynamic eccentricity [4], [5], [6]. There are many reasons lead to the eccentricity faults in rotating electric machines, and the air gap eccentricity in a electric motor can damage other components of the machine and cause breakdown of the machine if not corrected in time. During the manufacturing stage, it is impractical to make perfect motors with zero eccentricity. A small level of static eccentricity may exist due to the imperfect alignment between the stator core assembly and the rotation center, or the deviation of the stator core from a perfect circle. Similarly, a small dynamic eccentricity can also exist due to the imperfect alignment between center of the rotor and the rotation axis, or imperfect shape of the rotor. Throughout the operation of a motor, this eccentricity level can increase over time, for instance, due to the bearing degradation, or mechanical degradation of the mounting structure of the machine, which causes physical shift of the stator assembly and leads to eccentricity. The air gap eccentricity induces unbalanced magnetic pull, which may cause stator winding faults and rubbing between rotor and stator with the eccentricity level is high, eventually leads to machine failure without prompt maintenance. It is

therefore important to check electric motors for eccentricity in the manufacturing stage for quality control, and monitor the eccentricity level throughout the operation for safety and asset protection.

Many efforts have been put into the technology development of the eccentricity fault analysis and detection in the past a couple decades, with motor current signature analysis (MCSA) one major approach proposed for eccentricity fault detection [2], [7], [8], [9]. Compared with other methods such as vibration and acoustic sensing, MCSA has advantages of simple implementation and cost saving, as no additional sensors are required. When the air gap is non-uniform with eccentricity, additional harmonics will be introduced in the air gap permeance function and air gap flux combined with the rotor-generated MMF. Some of these harmonics will be reflected in the induced voltage in the stator windings, and eventually in the stator current. It is therefore theoretically possible to connect the eccentricity with certain frequency components in the stator current spectrum, making MCSA possible for eccentricity fault detection.

A lot of work has been dedicated to the detailed modeling and analysis of fault signatures for each type of eccentricity. Time-stepping finite-element simulation is a relatively accurate method to calculate the dynamic performance of the motor with eccentricity fault [10], [11]. However, such transient simulations are time consuming and computational intensive. Modified winding function method (MWFM) has been developed as an alternative technique for the analysis of electric machines [7], [12], [13]. Key features of MWFM are to describe the stator and rotor winding distributions with winding functions, describe the air gap distribution in the case of mechanical faults with a gap function, and compute the self and mutual inductance terms between all windings for each rotor position. Dynamic simulations with coupled-circuit model built on the MWFM can be used to obtain the stator current signals [14], where fault signatures can be revealed. However, due to simplifications in the modeling process, while past models can successfully identify the frequency components in the obtained stator current spectrum that are related to eccentricity fault, the exact amplitude of each fault component does not necessarily match with experiment results.

In this work, we improve the modeling process of an eccentric induction motor by taking the slotting effect and

saturation effect into consideration, and obtain the dynamic performance and stator current of different eccentricity conditions. We also build a test bench to conduct experiment measurements for the different eccentricity levels, and then quantitatively analyze and compare the frequency components of the stator current related to the eccentricity fault with data obtained from both MWFM based model and the experiment measurements, and show their good agreement across different eccentricity levels.

II. ECCENTRIC MOTOR MODELING METHOD

The MWFM is used to calculate the motor's inductance matrices. The inductance between a pair of windings at each time step can be calculated by the integration of the product of the two winding functions and the air gap permeance function, over all stator angles. For winding i and winding j , the inductance is derived as

$$L_{ij}(t) = \mu_0 l r \int_0^{2\pi} n_i(\phi, t) M_j(\phi, t) g^{-1}(\phi, t) d\phi, \quad (1)$$

where μ_0 is the vacuum permeability, r is air gap radius, l is the stack length, $n_i(\phi, t)$ is the winding turns function for winding i , and $M_j(\phi, t)$ is the modified winding function for winding j , which is calculated by

$$M(\phi, t) = n(\phi, t) - \langle M(t) \rangle, \quad (2)$$

where

$$\langle M(t) \rangle = \frac{1}{2\pi \langle g^{-1}(\phi, t) \rangle} \int_0^{2\pi} n(\phi, t) g^{-1}(\phi, t) d\phi, \quad (3)$$

$$\langle g^{-1}(\phi, t) \rangle = \frac{1}{2\pi} \int_0^{2\pi} g^{-1}(\phi, t) d\phi. \quad (4)$$

As we can see from the above equations, the air gap function is essential in calculating the motor performance especially under eccentricity conditions, and needs to be described accurately.

For an ideal slot-less motor, the air gap is uniform with nominal size denoted as g_0 . Static eccentricity makes the air gap asymmetric, and creates a time-invariant sinusoidal modulation to the air gap with amplitude given by δ_{SE} . Dynamic eccentricity, on the other hand, causes a time-varying modulation to the air gap, which is represented by another cosine function with amplitude δ_{DE} .

In addition, the slots in the stator and rotor effectively make the gap length larger than the nominal g_0 . A Carter's coefficient K_c is used to represent this increase of average gap size. The value of Carter's coefficient can be calculated from the geometrical parameters of the motor, especially the slots.

Last but not the least, due to the nonlinear magnetic properties of iron core of motors, the permeability of the iron core is not a constant, but drops at higher flux density. This saturation effect makes the effective air gap size smaller, and also adds a time-dependent modulation to the air gap function. A common way to describe the saturation effect is

to define a saturation factor k_{sat} as the ratio of fundamental components of the air gap voltage for motor at non-saturated and saturated conditions [15], [16]. The air gap modification due to saturation is describe as

$$g_s(\phi, t) = g_1 [1 - \rho \cos(2p\phi - 2\omega_r t)] \quad (5)$$

where p is the pole pair number, ϕ is the stator angle, ω_r is the rotation speed, g_1 is the mean value of air gap length under saturation,

$$g_1 = g_0 \frac{3k_{sat}}{k_{sat} + 2}, \quad (6)$$

and ρ is the peak value of air gap fluctuation due to saturation,

$$\rho = \frac{2(k_{sat} - 1)}{3k_{sat}} \quad (7)$$

After taking these effects into consideration, the air gap function is now described as:

$$g(\phi, t) = g_s K_c - \delta_{SE} g_0 \cos(\phi) - \delta_{DE} g_0 \cos(\phi - \omega_r t). \quad (8)$$

For dynamic simulation of the induction motor, the inductance terms are updated at each time step using the MWFM formulation. Coupled with the voltage, flux linkage, torque, and mechanical dynamics equations from circuit model, the full dynamic performance of the induction motor can be obtained.

For a three-phase squirrel-cage induction machine with rotor bar number R , the stator voltage and flux linkage are described by equations

$$V_s = R_s I_s + \frac{d}{dt} \Lambda_s, \quad (9)$$

$$\Lambda_s = L_{ss} I_s + L_{sr} I_r, \quad (10)$$

where $V_s = [v_{s1}, v_{s2}, v_{s3}]^T$ is the stator voltage, $I_s = [i_{s1}, i_{s2}, i_{s3}]^T$ is the stator current, $\Lambda_s = [\lambda_{s1}, \lambda_{s2}, \lambda_{s3}]^T$ is the stator flux linkage, $I_r = [i_{r1}, i_{r2}, \dots, i_{rR}, i_e]^T$ is a vector of length $R+1$ to describe rotor loop currents and the end ring current respectively. R_s is a 3×3 stator resistance matrix, L_{ss} is the 3×3 stator inductance matrix, and L_{sr} is the $3 \times (R+1)$ matrix containing mutual inductances between stator phases and rotor loops.

For the rotor side, the voltage equation and flux linkage equation are respectively

$$V_r = R_r I_r + \frac{d}{dt} \Lambda_r, \quad (11)$$

$$\Lambda_r = L_{rs} I_s + L_{rr} I_r, \quad (12)$$

where $L_{rs} = L_{sr}^T$, and L_{rr} is the $(R+1) \times (R+1)$ self-inductance matrix of the rotor loops. Note that for squirrel cage rotors, the rotor voltages are zero: $V_r = [0, 0, \dots, 0]^T$.

The torque equation of the induction motor is

$$T_e = \frac{1}{2} I_s^T \frac{\partial L_{ss}}{\partial \theta_r} I_s + I_s^T \frac{\partial L_{sr}}{\partial \theta_r} I_r + \frac{1}{2} I_r^T \frac{\partial L_{rr}}{\partial \theta_r} I_r, \quad (13)$$

where θ_r is the rotor's mechanical angle.

The mechanical dynamics of the motor is

$$\frac{d}{dt}\omega_r = \frac{1}{J}(T_e - T_L), \quad (14)$$

$$\frac{d}{dt}\theta_r = \omega_r, \quad (15)$$

where ω_r is the mechanical speed, T_L is the load torque, and J is the inertia of the rotor.

As we can see from the motor dynamic model, it is critical to obtain the inductance components in equations (10) and (12), and the inductance derivatives in equation (13). These values are computed using the MWFM models.

III. EXPERIMENT SETUP & DATA ACQUISITION

To validate the model accuracy, we conduct experiment measurements to obtain data from an eccentric induction motor. In this work, a 0.75 kW, three-phase squirrel-cage induction motor is used for the experimental study, with major parameters listed in Table I. The line-to-line voltage and frequency are 200 V and 60 Hz, respectively. As shown in Fig. 1, a few modifications are made to the motor to create different levels of eccentricity fault. The original bearings of the motor are removed, and the rotor is instead supported by two custom-made mounting structures (only the mount on the load side is visible in the photo) through the extended rotor shaft and a pair of new bearings installed on the mounting structures. The stator assembly of the motor is mounted on a linear stage with its position adjustable in the horizontal direction by two pairs of micrometers. Two pairs of displacement sensors are also installed on the stator facing air gap at the load side and opposite side respectively, to measure the actual air gap size in horizontal and vertical directions when the motor is operating. A power brake is connected to the test motor and serves as load.

TABLE I: Major Parameters of the Induction Motor

Parameter	Value
Number of pole pairs	2
Number of bars	28
Number of stator slots	36
Number of turns per slot	37
Nominal air gap length	0.28 mm
Air gap radius	41.6 mm
Stack length	80 mm

With the modified motor setup, different static eccentricity levels in the horizontal direction can be created. In our experiment, a total of 6 eccentricity levels were created when the motor is stand still; data from three phase current sensors and four air gap sensors were recorded for each eccentricity level at 10 kHz sampling frequency under no-load condition. The eccentricity levels were set at 1.5%, 17.2%, 24.1%, 40.5%, 47.1%, 64.6% respectively, with percentage defined as the ratio of the maximum air gap deviation and the nominal air gap size. From the air gap sensor readings shown in Fig. 2(a) and (b), we see that the actual static eccentricity level, represented by the

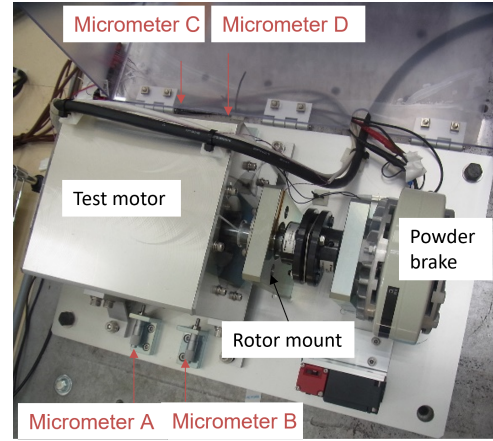


Fig. 1: The experiment setup for the study of induction motor eccentricity.

vertical offset, is close to the pre-set values, while there is also periodic oscillations, representing a small dynamic eccentricity level. The static eccentricity occurs mostly in the x-direction, while there is a small static eccentricity in y-direction. In addition, there are slight differences in the two sets of sensor readings on the load side and opposite side, indicating a small misalignment of the setup.

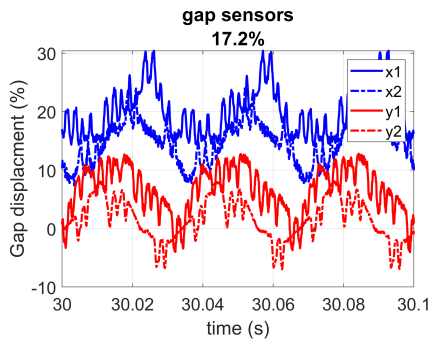
We then extract the actual static and dynamic eccentricity levels from the gap sensor readings for all cases, and plot them in Fig. 2(d) and (d). As we can see, the actual static eccentricity of the air gap is very close to the initial settings, with difference within 3% in all cases. In addition, a small dynamic eccentricity level of around 6% exists for all cases according to air gap sensor readings. This mixed eccentricity effect create a side band signal at $f_c = f_s \pm f_r$, where f_s is the supply frequency and f_r is the rotation frequency.

IV. RESULTS & DISCUSSIONS

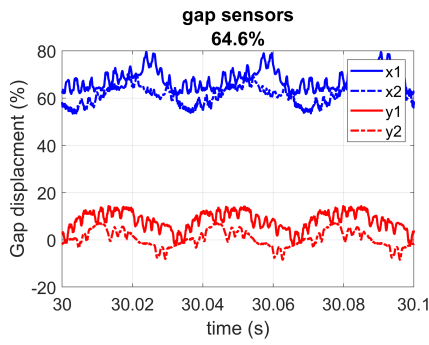
Before running simulation with the MWFM based model, we need to determine the Carter's coefficient and saturation factor values. While there are different ways to identify their values, we determine the two factors with the assist of finite-element simulations in this work.

To identify Carter's coefficient, we build 2d model based on the CAD drawing of the induction motor, and run linear 2d finite-element simulation, under no-load and no eccentricity fault, using core material of fixed permeability ($\mu_r = 3,000$). We then compare the obtained stator current amplitude from MWFT based model with different Carter's coefficient values and those obtained from the linear finite-element simulation. With carter's coefficient $K_c = 1.40$, the MWFT model result for phase current amplitude matches with the linear finite-element simulation result.

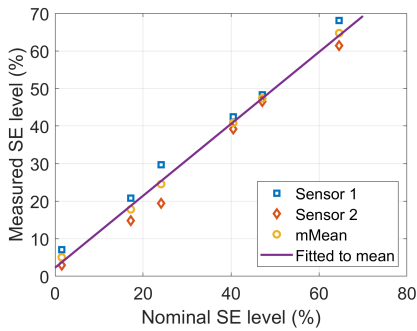
To identify saturation factor, we further run nonlinear finite-element simulation using the B-H curve from the actual iron core material. We then compare the phase current result from the MWFM based model using different saturation factor values with the nonlinear finite-element simulation result. As



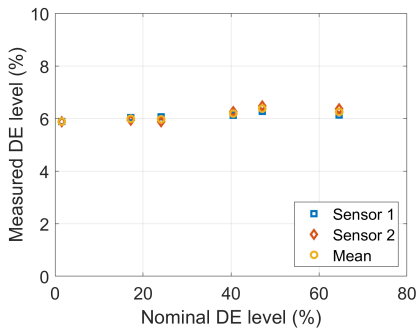
(a)



(b)



(c)



(d)

Fig. 2: The time-domain gap sensor readings for two pre-set eccentricity levels (a) 17.2% and (b) 64.6%. (c) The extracted (c) static eccentricity level and (d) dynamic eccentricity level from gap sensor readings as function of the pre-set static eccentricity level.

shown in Fig. 3(a), the stator current amplitude increases when the iron core permeability in the finite-element simulation is changed from linear to nonlinear. As a result, some parts of the core saturates even at no-load condition, which makes the effective permeability lower than in the linear region, and

With $k_{sat} = 1.60$, the phase current amplitude from the model matches with the nonlinear finite-element simulation result.

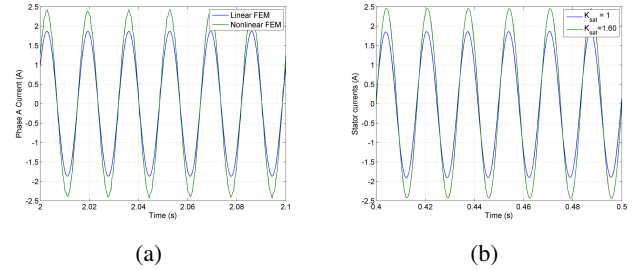


Fig. 3: The time-domain gap sensor readings for two pre-set eccentricity levels (a) 17.2% and (b) 64.6%. (c) The extracted (c) static eccentricity level and (d) dynamic eccentricity level from gap sensor readings as function of the pre-set static eccentricity level.

With all the input parameters determined, we now run dynamic simulations under different eccentricity conditions. Based on the experiment measurement of the air gap profile, we add 6% dynamic eccentricity in the MWFM based simulations, and run simulations for different eccentricity levels every 10% from 0% to 70% under no-load condition. Fig. 4 shows the simulated stator current time-domain data and frequency spectrum from Fourier transform, along with experimental measurement results, for the case of 40% static eccentricity. As you can see, the modeled results agree very well with experiment results, in both time-domain and frequency-domain data.

An important component in the stator current spectrum due to mixed eccentricity fault is the side band signal at $f_c = f_s \pm f_r$, where f_s is the supply frequency and f_r is the rotation frequency. In our experiment $f_s = 60$ Hz, and f_c is close to 30 Hz. As shown in Fig. 4(f) from experiment data, the two side bands around 30 Hz and 90 Hz are significant. And the MWFM based model result show similar behavior as shown in Fig. 4(e). Results at other eccentricity levels are also matching well between simulations and experiment measurements.

To study the evolution of eccentricity fault and how we can detect and quantify the fault level from stator current, we use the power ratio of the $f_s - f_c$ side band and the fundamental frequency f_s as a fault indicator. We obtain values of the fault indicator for motor with different eccentricity fault levels from both experiment and simulation stator current data, and the results are shown in Fig. 5. As expected, the amplitude of the fault indicator increases monotonically with the increasing eccentricity fault level. As a matter of fact, the amplitude of the fault component is proportional to the corresponding magnetic flux component generated due to the fault. Since the magnetic

flux is the product of the air gap permeance and the rotor generated MMF, both of which are linearly proportional to the eccentricity fault level [17], [18], the fault component should be a quadratic function of the fault level. In Fig. 5, we fit simulation results and experiment results respectively with a quadratic function to show the trend of the fault indicator with increasing eccentricity fault level.

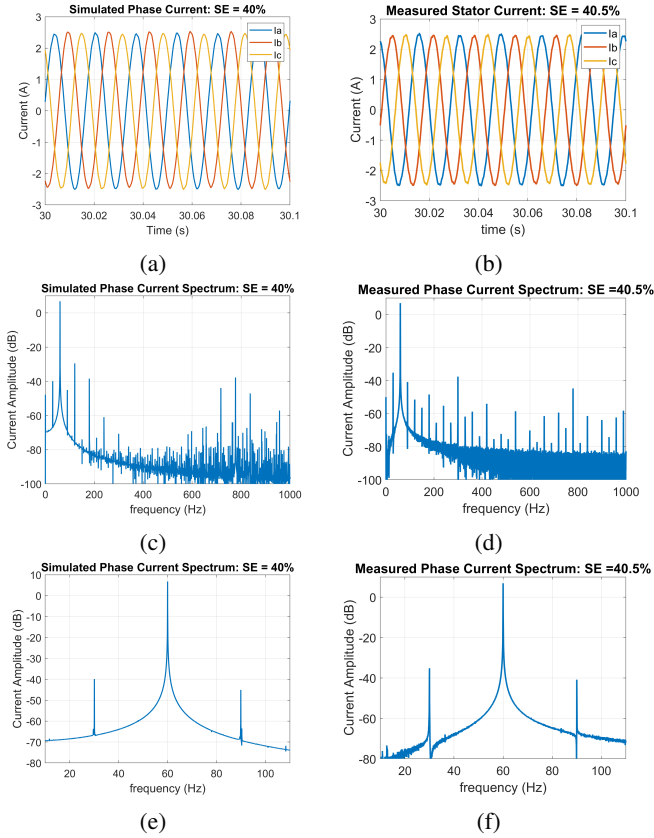


Fig. 4: Simulated and measured stator (a) & (b) current time-domain signal, (c) & (d) frequency spectrum, and (e) & (f) low-frequency end of the stator current spectrum for static eccentricity level 40%.

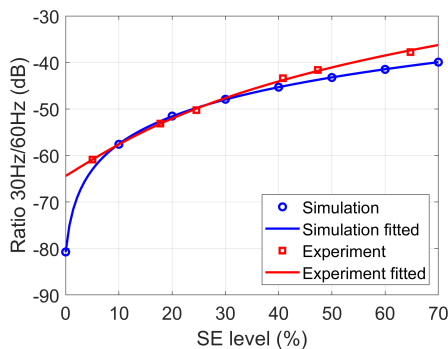


Fig. 5: Comparison between simulation and experiment of the extracted side band amplitude, as a function of static eccentricity level.

Comparing the results between the experiment and simulation results, we can see that the two curve agree well with each other, especially when the eccentricity level is low. The experiment values of the fault indicator are higher than the simulation results at higher eccentricity levels, due to the contributions from other factors in the experiment setup, such as the misalignment in the axial direction, increased vibration level causing additional air gap variation, etc. When the eccentricity level is higher than 50%, the rotor may start rubbing the stator, which may eventually cause damages or even failures of the machine, and also contributes to the differences between simulation and experiment. For the purpose of fault detection, it is more important to be able to detect accurately when the fault is at early stage and the fault signal is relatively small.

For condition monitoring and condition-based maintenance of electric machines based on MCSA method, we envision that fault components in the stator current of the machines that correspond to different fault types are regularly monitored and compared against pre-determined threshold values; maintenance requests for corresponding faulty components are triggered if the monitored fault indicators exceed the threshold values. To achieve that, proper threshold values need to be identified for each component and each electric machine. As there can be many machines of different power ratings that are operating at the same plant, each with varying speed and load conditions, the fault component values for different machines and different conditions also vary. The quantitative MWFM based model includes the electrical parameters of the electric machine, accounts for different mechanical faults with changing air gap profile, and can simulate the dynamic operation of electrical machine with different load conditions as well.

V. CONCLUSIONS

In this paper, we investigated the accurate modeling of induction motor with eccentricity fault based on coupled-circuit model and modified winding function method. The eccentricity fault is described by the time-invariant and time-varying periodic modulations of the air gap profile of the motor. Slotting effect and saturation effect were taken into consideration to improve the accuracy of the model. We showed that the motor dynamics can be simulated and the stator current spectrum can be obtained from the model, and fault signatures of eccentricity fault can be extracted. The modelled results agree well with experiment measurements at different eccentricity levels. For motor condition monitoring and condition-based maintenance using motor current signature analysis method, this model helps track the fault level and set proper threshold values for maintenance needs.

REFERENCES

- [1] M. E. H. Benbouzid, "A review of induction motors signature analysis as a medium for faults detection," *IEEE transactions on industrial electronics*, vol. 47, no. 5, pp. 984–993, 2000.

- [2] S. Nandi, H. A. Toliyat, and X. Li, "Condition monitoring and fault diagnosis of electrical motors—a review," *IEEE transactions on energy conversion*, vol. 20, no. 4, pp. 719–729, 2005.
- [3] H. A. Toliyat, S. Nandi, S. Choi, and H. Meshgin-Kelk, *Electric machines: modeling, condition monitoring, and fault diagnosis*. CRC press, 2012.
- [4] S. Nandi, R. M. Bharadwaj, and H. A. Toliyat, "Performance analysis of a three-phase induction motor under mixed eccentricity condition," *IEEE Transactions on Energy Conversion*, vol. 17, no. 3, pp. 392–399, 2002.
- [5] X. Li, Q. Wu, and S. Nandi, "Performance analysis of a three-phase induction machine with inclined static eccentricity," *IEEE Transactions on Industry Applications*, vol. 43, no. 2, pp. 531–541, 2007.
- [6] W. T. Thomson and I. Culbert, *Current signature analysis for condition monitoring of cage induction motors: Industrial application and case histories*. John Wiley & Sons, 2017.
- [7] S. Nandi, S. Ahmed, and H. A. Toliyat, "Detection of rotor slot and other eccentricity related harmonics in a three phase induction motor with different rotor cages," *IEEE Transactions on Energy Conversion*, vol. 16, no. 3, pp. 253–260, 2001.
- [8] K. N. Gyftakis and J. C. Kappatou, "A novel and effective method of static eccentricity diagnosis in three-phase psh induction motors," *IEEE Transactions on Energy Conversion*, vol. 28, no. 2, pp. 405–412, 2013.
- [9] M. Akar, "Detection of a static eccentricity fault in a closed loop driven induction motor by using the angular domain order tracking analysis method," *Mechanical Systems and Signal Processing*, vol. 34, no. 1–2, pp. 173–182, 2013.
- [10] J. Faiz, B. M. Ebrahimi, B. Akin, and H. A. Toliyat, "Comprehensive eccentricity fault diagnosis in induction motors using finite element method," *IEEE Transactions on Magnetics*, vol. 45, no. 3, pp. 1764–1767, 2009.
- [11] A. Sapena-Bano, M. Riera-Guasp, J. Martinez-Roman, M. Pineda-Sanchez, R. Puche-Panadero, and J. Perez-Cruz, "Fem-analytical hybrid model for real time simulation of ims under static eccentricity fault," in *2019 IEEE 12th International Symposium on Diagnostics for Electrical Machines, Power Electronics and Drives (SDMPED)*. IEEE, 2019, pp. 108–114.
- [12] N. A. Al-Nuaim and H. Toliyat, "A novel method for modeling dynamic air-gap eccentricity in synchronous machines based on modified winding function theory," *IEEE Transactions on energy conversion*, vol. 13, no. 2, pp. 156–162, 1998.
- [13] L. Zhou, B. Wang, C. Lin, H. Inoue, and M. Miyoshi, "Static eccentricity fault detection for psh-type induction motors considering high-order air gap permeance harmonics," in *2021 IEEE International Electric Machines & Drives Conference (IEMDC)*. IEEE, 2021, pp. 1–7.
- [14] X. Luo, Y. Liao, H. A. Toliyat, A. El-Antably, and T. A. Lipo, "Multiple coupled circuit modeling of induction machines," *IEEE Transactions on industry applications*, vol. 31, no. 2, pp. 311–318, 1995.
- [15] J. C. Moreira and T. A. Lipo, "Modelling of saturated ac machines including air gap flux harmonic components," *Conference Record of the 1990 IEEE Industry Applications Society Annual Meeting*, pp. 37–44 vol.1, 1990.
- [16] J. Faiz and B. M. Ebrahimi, "Static eccentricity fault diagnosis in an accelerating no-load three-phase saturated squirrel-cage induction motor," *Progress in electromagnetics research*, vol. 10, pp. 35–54, 2008.
- [17] L. Zhou, B. Wang, C. Lin, H. Inoue, and M. Miyoshi, "Static eccentricity fault detection for psh-type induction motors considering high-order air gap permeance harmonics," in *2021 IEEE International Electric Machines Drives Conference (IEMDC)*, 2021, pp. 1–7.
- [18] D. Dorrell, W. Thomson, and S. Roach, "Analysis of airgap flux, current, and vibration signals as a function of the combination of static and dynamic airgap eccentricity in 3-phase induction motors," *IEEE Transactions on Industry Applications*, vol. 33, no. 1, pp. 24–34, 1997.